

Real-time optical spike-timing dependent plasticity in a single VCSEL with dual-polarized pulsed optical injection

Shuiying XIANG^{1,2*}, Yanan HAN¹, Xingxing GUO¹, Aijun WEN¹,
Genquan HAN² & Yue HAO²

¹State Key Laboratory of Integrated Service Networks, Xidian University, Xi'an 710071, China;

²State Key Discipline Laboratory of Wide Bandgap Semiconductor Technology, School of Microelectronics, Xidian University, Xi'an 710071, China

Received 3 January 2020/Revised 7 February 2020/Accepted 27 February 2020/Published online 9 May 2020

Abstract We propose and numerically realize an optical spike-timing dependent plasticity (STDP) scheme by using a single vertical-cavity surface-emitting laser (VCSEL). In the scheme, the VCSEL is subjected to an orthogonally-polarized continuous-wave optical injection (OPCWOI) and dual-polarized pulsed optical injections (DPPOI). Based on the widely used spin-flip model, the response spiking dynamics of VCSEL is numerically studied, and then the optical STDP in a single VCSEL is explored. The roles of bias current, the strength of OPCWOI and DPPOI, and the frequency detuning on the optical STDP curve are numerically analyzed. It is found that, by simultaneously utilizing the response spiking dynamics in two orthogonal polarization modes, an optical STDP could be achieved by using a single VCSEL. Furthermore, the weight update of STDP curve can be calculated in real-time. Additionally, the STDP curves can also be controlled by adjusting some controllable parameters. The real-time optical STDP based on a single VCSEL is numerically realized for the first time, which paves the way towards fully VCSELs-based photonic neuromorphic systems with low power consumption.

Keywords vertical-cavity surface-emitting laser, optical spike-timing dependent plasticity, neuromorphic photonic system, dual polarized pulsed optical injections, artificial intelligent systems

Citation Xiang S Y, Han Y N, Guo X X, et al. Real-time optical spike-timing dependent plasticity in a single VCSEL with dual-polarized pulsed optical injection. *Sci China Inf Sci*, 2020, 63(6): 160405, <https://doi.org/10.1007/s11432-020-2820-y>

1 Introduction

The emerging ultra-fast neuromorphic computing system based on optical platform has attracted more and more attentions in recent years [1–9] (see [1] for a review), as it outperforms the conventional von Neumann approach for some special tasks, such as decision making and pattern recognition. Tremendous efforts have been directed toward the designing of photonic neurons that are the essential constituents and prerequisites for implementing ultrafast neuromorphic photonic computing systems [10–32].

Vertical-cavity surface-emitting lasers (VCSELs) have become promising candidates for photonic spiking neurons owing to the advantages of low manufacturing cost, low power consumption, easy implementation of large-scale integration, and rich polarization dynamics [10, 13, 18, 21–23, 27–30, 33]. It has been demonstrated both numerically and experimentally that, the VCSEL with a single-polarized pulsed optical injection (SPPOI) may exhibit neuron-like excitatory spiking dynamics [10, 13, 18, 21–23]. In addition,

* Corresponding author (email: jxxsy@126.com)

the generation as well as the propagation of inhibitory spiking dynamics have also been demonstrated in VCSELs [21,29,30]. Moreover, when a VCSEL is subjected to an orthogonally-polarized continuous-wave optical injection (OPCWOI) as well as a SPPOI, it has been numerically predicted that the unwanted relaxation oscillation after the excitatory spiking dynamics could be suppressed, which is helpful for the successful propagation of the neuron-like spiking dynamics [27]. The previous studies mainly involved the spiking dynamics of VCSEL when it is subjected to a single perturbation. Interestingly, it is found that shorter polarization switching time could be achieved by using a VCSEL which is subjected to dual polarized pulsed optical injections (DPPOI) [34]. However, the spiking response dynamics in a VCSEL that is subjected to multiple perturbations remains largely unexplored, especially when the stimuli pulses are close in time.

Concurrently, there are a variety of reports on the photonic devices and systems enabling the implementation of the spike-timing dependent plasticity (STDP), which is a prevalent protocol for synaptic weight update in spiking neural network [35–42]. For instance, Fok et al. [37] demonstrated an optical STDP circuit by simultaneously using a commercially available semiconductor optical amplifier (SOA) as well as an electro-absorption modulator. In their proposed scheme, the synaptic weight update could be immediately determined once a time difference is given. That is to say, the optical STDP is realized in real-time by two key devices. Besides, a real-time optical STDP has also been experimentally demonstrated by simultaneously using two twin SOAs [39]. In addition, there is a report on realization of optical STDP in a single SOA [40,41]. However, to obtain the STDP curve with both positive and negative synaptic weight update amounts, a reference output power of SOA extracted from a given time difference is required to calculate the weight update for each time difference. As a result, the optical STDP could not be realized in real-time by using a single key device. In our previous study, we numerically predicted that the vertical-cavity semiconductor optical amplifier (VCSSOA) could provide a feasible solution for optical STDP with much lower bias current and optical input power compared with the conventional SOA-based schemes [42]. Nonetheless, the synaptic weight update amount is determined after recording all the output powers of VCSSOA for each time difference within the learning window and by utilizing the maximum power as a reference value. In other words, the optical STDP could not be realized in real-time in a single VCSSOA. To date, the real-time optical STDP achieved in a single device still remains a challenge, which is highly desirable for the on-line learning in the future ultrafast neuromorphic photonic computing systems.

In this study, we propose to implement a real-time optical STDP in a single VCSEL by introducing both OPCWOI and DPPOI. Hence, a versatile photonic spiking neural network consisting of polarization switching VCSELs, which guarantee both the generation of spiking dynamics as well as the implementation of optical STDP, can be expected. The remainder of this study is organized as follows. Section 2 presents the theoretical model of a VCSEL that is subjected to OPCWOI and DPPOI. In Section 3, the response spiking dynamics of a VCSEL and the real-time optical STDP implemented in the VCSEL are carefully studied. The effects of the bias current, the strength of OPCWOI and DPPOI, and the frequency detuning on the optical STDP properties are examined. At last, we present the conclusion in Section 4.

2 Theory and model

A schematic diagram for the proposed optical STDP circuit based on a single VCSEL is illustrated in Figure 1. In this scheme, E_{cwx} represents the OPCWOI, whose strength can be adjusted by a variable optical attenuator (VOA). Here, the OPCWOI is introduced to induce a normal polarization switching effect, and thus, to trigger the spiking dynamics based on the transition between two injection-locked states [27]. The pre- and post-synaptic spikes, which are fired by two photonic spiking neurons in a possible photonic neural network, are represented by E_{injx} and $E_{in jy}$. Here, the stimulus pulse E_{injx} is injected into x-polarization (XP) mode of VCSEL, while the stimulus pulse $E_{in jy}$ is injected into the y-polarization (YP) mode. The variable-optical delay line (VODL) is employed to adjust the time

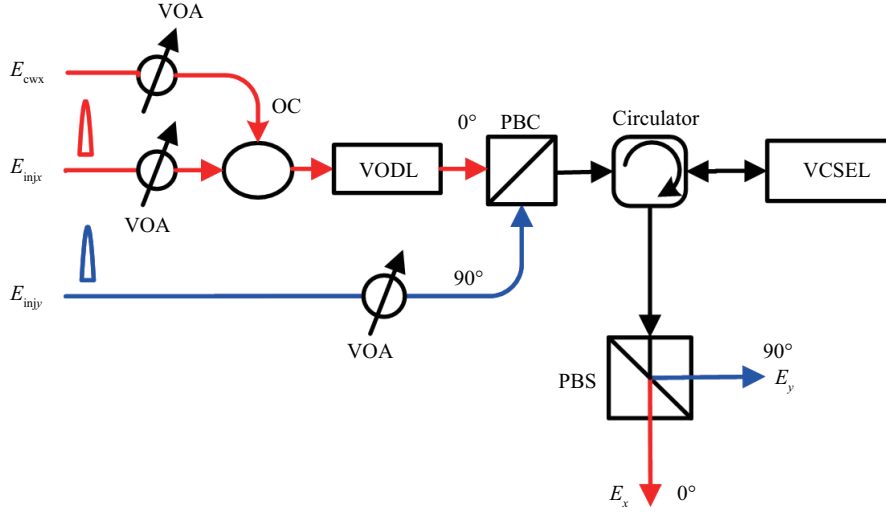


Figure 1 (Color online) A schematic illustration of real-time optical STDP based on a single VCSEL with DPPOI and OPCWOI. E_{cwx} represents OPCWOI; E_{injx} and E_{injy} denote the stimuli pulses; VOA is variable optical attenuator; OC means optical coupler; VODL represents variable optical delay line; PBC (PBS) denotes polarization beam combiner (splitter).

difference between E_{injx} and E_{injy} . The OPCWOI and DPPOI are injected into the VCSEL through a polarization beam combiner (PBC) and an optical circulator. Finally, the two orthogonal polarization modes separated by a polarization beam splitter (PBS) are both utilized to calculate the weight update amount at each time difference for the real-time optical STDP. The spin-flip model (SFM) has been widely employed to numerically investigate the polarization dynamical properties of a VCSEL. It includes the rate equations for amplitude of XP (YP) mode E_x (E_y), total carrier inversion N , and difference between carrier inversions with opposite spins n . To incorporate both the OPCWOI and DPPOI, the modified rate equations are described as follows [27, 34, 43–50]:

$$\begin{aligned} \frac{dE_x(t)}{dt} = & k(1 + i\alpha)[(N - 1)E_x + inE_y] - (\gamma_a + i\gamma_p)E_x + k_{cwx}E_{cwx}e^{i\Delta_{cwx}t} \\ & + k_{injx}(t)e^{i\Delta_x t} + \sqrt{\frac{\beta_{sp}\gamma_N}{2}}[\sqrt{(N+n)}\xi_+(t) + \sqrt{(N-n)}\xi_-(t)], \end{aligned} \quad (1)$$

$$\begin{aligned} \frac{dE_y(t)}{dt} = & k(1 + i\alpha)[(N - 1)E_y + inE_x] - (\gamma_a + i\gamma_p)E_y + k_{injx}(t)e^{i\Delta_x t} \\ & + i\sqrt{\frac{\beta_{sp}\gamma_N}{2}}[\sqrt{(N-n)}\xi_-(t) - \sqrt{(N+n)}\xi_+(t)], \end{aligned} \quad (2)$$

$$\frac{dN}{dt} = \gamma_N[\mu - N(1 + |E_x|^2 + |E_y|^2) + in(E_x E_y^* - E_y E_x^*)], \quad (3)$$

$$\frac{dn}{dt} = -\gamma_s n - \gamma_N[n(|E_x|^2 + |E_y|^2) + iN(E_y E_x^* - E_x E_y^*)]. \quad (4)$$

In these equations, the internal parameters of VCSEL include the field decay rate k , the linear dichroism (birefringence) γ_a (γ_p), the spin-flip rate γ_s , the decay rate of N represented by γ_N , and the linewidth enhancement factor denoted by α . μ represents the normalized bias current ($\mu = 1$ means threshold current), and is an important external controllable parameter. The OPCWOI is determined by the amplitude E_{cwx} and angular frequency difference $\Delta\omega_{cwx}$. The DPPOI is represented by amplitudes $E_{injx}(t)$ and $E_{injy}(t)$, as well as angular frequency differences $\Delta\omega_x$ and $\Delta\omega_y$. Here, the stimulus pulse (perturbation) is simply used by a Gaussian pulse whose full-width at half-maximum is 20 ps. We define the timing of peak location of two stimuli Gaussian pulses as t_x and t_y for E_{injx} and E_{injy} , respectively. The time difference between two stimuli pulses is defined as $\Delta t = t_x - t_y$. k_{injx} and k_{injy} stand for the stimuli strength of DPPOI. For simplicity, we assume $k_{cwx} = k_{injx}$, $\Delta\omega_{cwx} = \Delta\omega_x$. We introduce angular

frequency differences as $\Delta\omega_x = \omega_{\text{inj}x} - \omega_0$, $\Delta\omega_y = \omega_{\text{inj}y} - \omega_0$, where $\omega_0 = (\omega_x + \omega_y)/2$ is the center frequency of two orthogonal polarization modes, and $\omega_x = \omega_0 + \alpha\gamma_a - \gamma_p$, $\omega_y = \omega_0 + \gamma_p - \alpha\gamma_a$. The frequency detuning between two stimuli pulses, i.e., $E_{\text{inj}x}$ and $E_{\text{inj}y}$, is defined as $\Delta f_{\text{inj}yx} = f_{\text{inj}y} - f_{\text{inj}x}$. $\Delta f_x = f_{\text{inj}x} - f_x$ represents the frequency difference between $E_{\text{inj}x}$ and the XP mode. In this way, one can get $\Delta\omega_x = 2\pi\Delta f_x + \alpha\gamma_a - \gamma_p$ and $\Delta\omega_y = 2\pi[\Delta f_{\text{inj}yx} + \Delta f_x + (\alpha\gamma_a - \gamma_p)/\pi] + \gamma_p - \alpha\gamma_a$. The last terms in (1) and (2) stand for spontaneous emission noise, where β_{sp} represents the noise strength, $\xi_+(t)$ and $\xi_-(t)$ are complex Gaussian noise. The mean value of the Gaussian noise is zero, and the time correlation satisfies $\langle \xi_i(t)\xi_j^*(\dot{t}) \rangle = 2\delta_{ij}\delta(t - \dot{t})$. The above rate equations are numerically solved with typical parameters of an 850 nm VCSEL [27]: $\alpha = 3$, $k = 300 \text{ ns}^{-1}$, $\gamma_a = 0.5 \text{ ns}^{-1}$, $\gamma_N = 1 \text{ ns}^{-1}$, $\gamma_p = 30 \text{ ns}^{-1}$, $\gamma_s = 50 \text{ ns}^{-1}$ and $\beta_{sp} = 10^{-4}$. For a solitary VCSEL, the YP mode is the only lasing mode for $\mu \leq 1.4$ while both XP and YP modes coexist for $\mu > 1.4$. The following parameters are fixed at $\mu = 1.5$, $k_{\text{inj}x} = k_{\text{inj}y} = 100 \text{ ns}^{-1}$, $\Delta f_x = -5 \text{ GHz}$, $\Delta f_{\text{inj}yx} = 0 \text{ GHz}$, $\Delta t = 0.5 \text{ ns}$, unless otherwise stated.

3 Numerical results and discussion

We firstly discuss the response spiking dynamics of a single VCSEL subject to OPCWOI and DPPOI. Then, we explore the realization of optical STDP based on the response spiking dynamics in two polarization modes of a single VCSEL. Furthermore, the effects of the strength of OPCWOI, bias current of VCSEL, stimuli strength of DPPOI, as well as two defined frequency detuning, i.e., Δf_x and $\Delta f_{\text{inj}yx}$, on the real-time optical STDP properties are numerically examined.

3.1 Response spiking dynamics of VCSEL subject to OPCWOI and DPPOI

At first, we consider the response spiking dynamics in XP and YP modes under different conditions to determine the diversity operating regimes. The intensities are calculated by $I_{x,y}(t) = |E_{x,y}(t)|^2$. The input stimuli pulses are presented in Figures 2(a) and (f). As shown in Figure 2(b), the solitary VCSEL is operated in the YP mode. If a short stimulus pulse $E_{\text{inj}y}$ shown in Figure 2(a) is introduced, as presented in Figure 2(c), an output spike is generated, and unwanted relaxation oscillations are observed after the termination of the stimulus pulse. When the E_{cwx} is introduced, we obtain $I_y > I_x$ as observed in Figure 2(d). This can be attributed to the polarization switching induced by the injection-locking effect [27]. If both $E_{\text{inj}y}$ and E_{cwx} are injected into the VCSEL, it can be observed from Figure 2(e), within the duration of the stimulus pulse, an output spike can also be triggered. Moreover, there is no relaxation oscillation after the spike, which is attributed to the transition between two different injection-locked states [27]. On the other hand, when $E_{\text{inj}x}$ and $E_{\text{inj}y}$ presented in Figure 2(f) corresponding to two stimuli pulses close in time are applied to the VCSEL, as can be seen from Figures 2(g)–(j), the VCSEL exhibits response spiking dynamics that is closely related to E_{cws} . For $E_{\text{cws}} = 0$, unwanted relaxation oscillations are observed after the termination of the two stimuli pulses. Interestingly, for the case of $E_{\text{cws}} \neq 0$, the maximum values of generated spikes also vary with E_{cws} . For convenience, they are denoted as I_{xm} and I_{ym} . As can be clearly seen from Figures 2(h)–(j), when $E_{\text{cws}} = 0.65$, $I_{xm} < I_{ym}$, when $E_{\text{cws}} = 0.5$, $I_{xm} \approx I_{ym}$, while for $E_{\text{cws}} = 0.8$, $I_{xm} > I_{ym}$.

Next, we focus on the case for which the DPPOI and OPCWOI are all injected into the VCSEL. The values of I_{xm} and I_{ym} as functions of E_{cws} are presented in Figure 3. For clarity, we denote the critical value of E_{cws} corresponding to $I_{xm} \approx I_{ym}$ as the PS point. It can be seen that, when the E_{cws} is smaller than the PS point, we obtain $I_{xm} < I_{ym}$. But for E_{cws} that is greater than the PS point, we get $I_{xm} > I_{ym}$. Namely, the spike generated in the XP mode is larger. Besides, the value of E_{cws} corresponding to the PS point is smaller for a larger $\Delta f_{\text{inj}yx}$. More precisely, these PS points locate at $E_{\text{cws}} = 1$, $E_{\text{cws}} = 0.6$, $E_{\text{cws}} = 0.45$, and $E_{\text{cws}} = 0.35$, for $\Delta f_{\text{inj}yx} = -5 \text{ GHz}$, $\Delta f_{\text{inj}yx} = 0 \text{ GHz}$, $\Delta f_{\text{inj}yx} = 5 \text{ GHz}$, and $\Delta f_{\text{inj}yx} = 10 \text{ GHz}$, respectively.

In order to identify the PS points, the two-dimensional maps of I_{xm} and I_{ym} are further presented in Figure 4 for different combinations of μ and E_{cws} . The values of the intensity difference $I_{xm} - I_{ym}$ are also provided. The dashed line corresponding to $I_{xm} - I_{ym} = 0$ is presented to highlight the PS points.

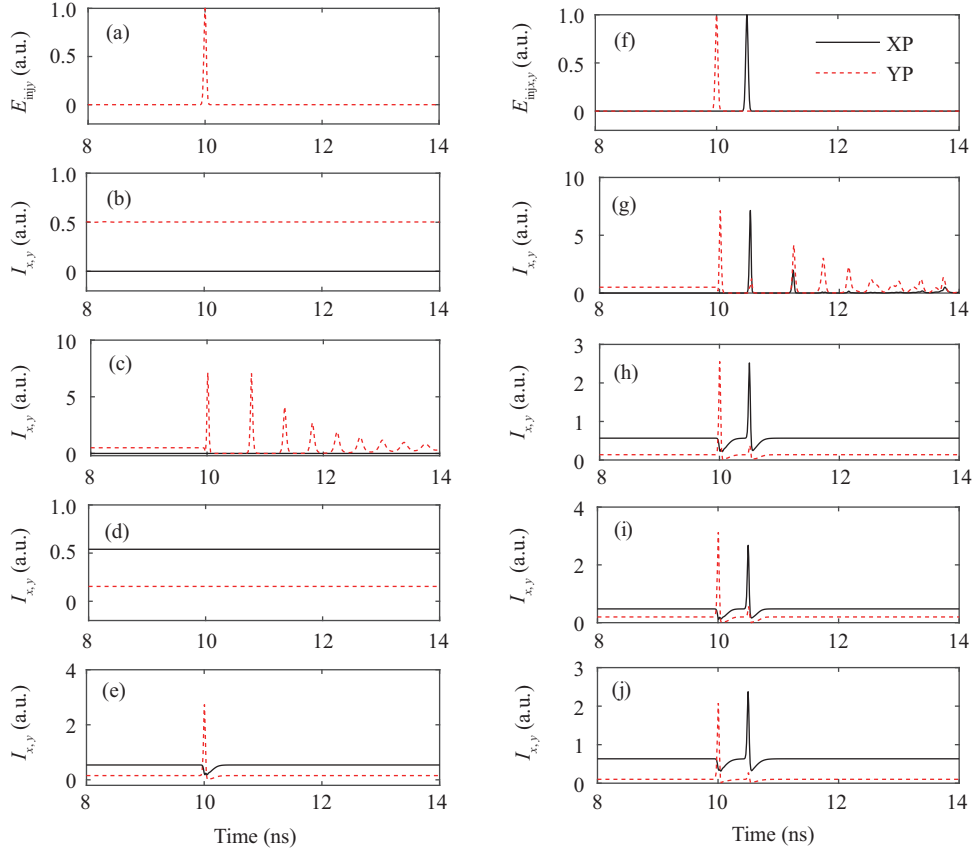


Figure 2 (Color online) Stimuli pulses ((a), (f)) and the responses ((b)–(e), (g)–(j)) of VCSEL under different conditions, (b) $E_{cwX} = 0$, $k_{injX} = k_{injY} = 0$, (c) $E_{cwX} = 0$, $k_{injX} = 0$, $k_{injY} = 100 \text{ ns}^{-1}$, (d) $E_{cwX} = 0.65$, $k_{injX} = k_{injY} = 0$, (e) $E_{cwX} = 0.65$, $k_{injX} = 0$, $k_{injY} = 100 \text{ ns}^{-1}$, (g) $E_{cwX} = 0$, $k_{injX} = k_{injY} = 100 \text{ ns}^{-1}$, (h) $E_{cwX} = 0.65$, $k_{injX} = k_{injY} = 100 \text{ ns}^{-1}$, (i) $E_{cwX} = 0.5$, $k_{injX} = k_{injY} = 100 \text{ ns}^{-1}$, (j) $E_{cwX} = 0.8$, $k_{injX} = k_{injY} = 100 \text{ ns}^{-1}$.

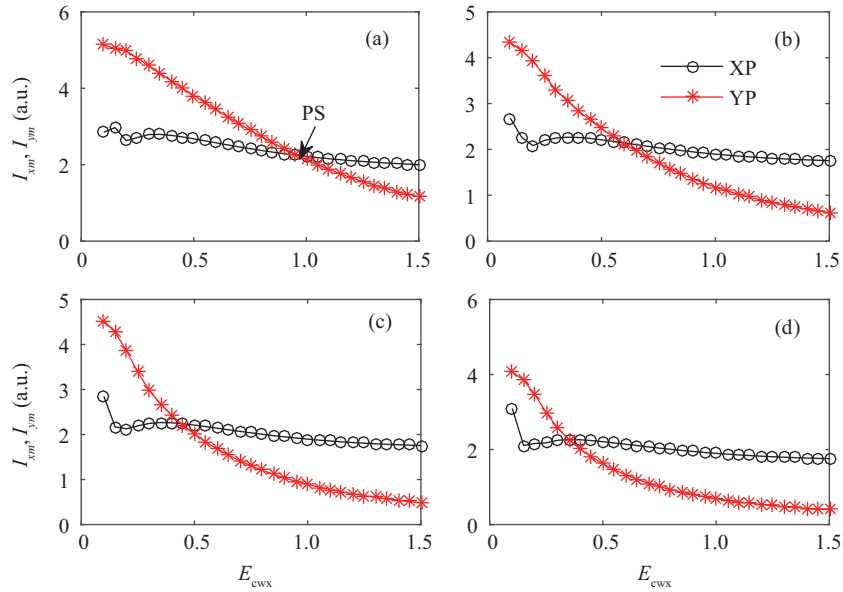


Figure 3 (Color online) I_{xm} and I_{ym} as functions of E_{cwX} for different cases of Δf_{injYX} . (a) $\Delta f_{injYX} = -5 \text{ GHz}$, (b) $\Delta f_{injYX} = 0 \text{ GHz}$, (c) $\Delta f_{injYX} = 5 \text{ GHz}$, (d) $\Delta f_{injYX} = 10 \text{ GHz}$.

It can be seen that, the E_{cws} corresponding to the PS point is larger for a higher μ . Besides, for different values of Δf_{injYX} , the overall trends are similar. It can also be found that, for a given μ , the PS points

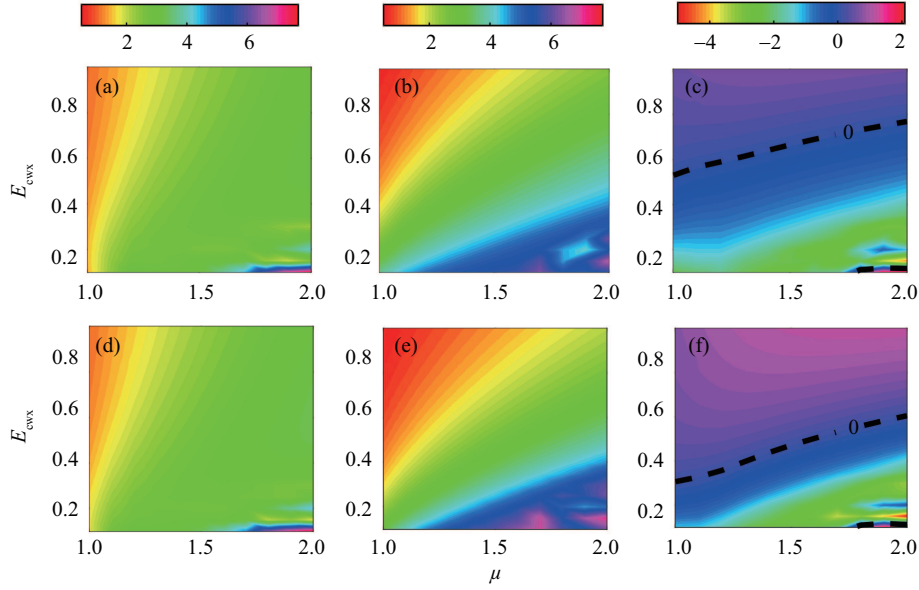


Figure 4 (Color online) Two-dimensional maps of I_{xm} (left column), I_{ym} (middle column), $I_{xm} - I_{ym}$ (right column) for different combinations of E_{cwx} and μ . (a)–(c) $\Delta f_{injyx} = 0$ GHz, $\Delta f_x = -5$ GHz, (d)–(f) $\Delta f_{injyx} = 5$ GHz, $\Delta f_x = -5$ GHz.

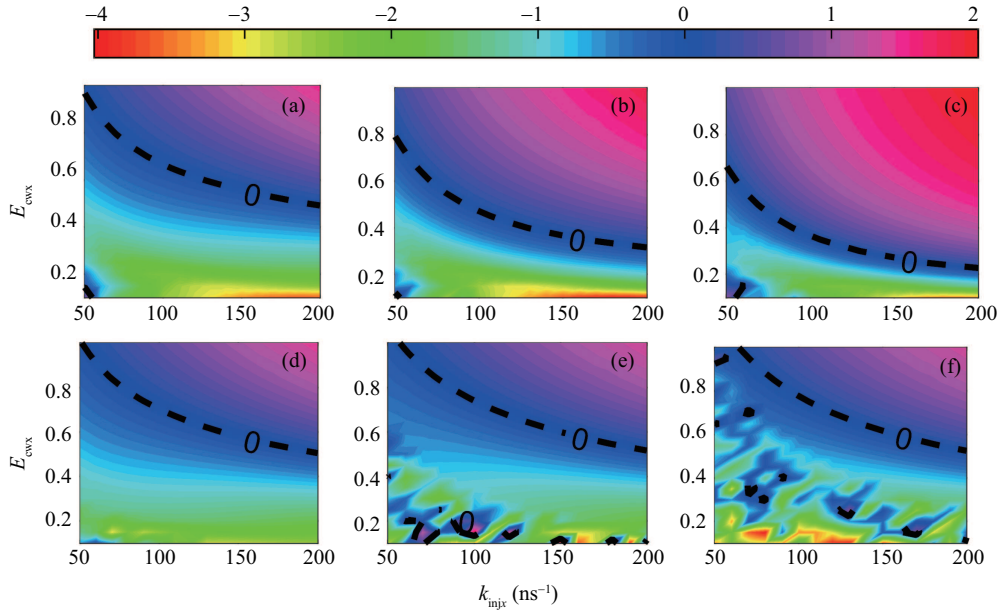


Figure 5 (Color online) Two-dimensional maps of $I_{xm} - I_{ym}$ for different combinations of k_{injx} and E_{cwx} . (a)–(c) $\Delta f_x = -5$ GHz, (d)–(f) $\Delta f_{injyx} = 0$ GHz, (a) $\Delta f_{injyx} = 0$ GHz, (b) $\Delta f_{injyx} = 5$ GHz, (c) $\Delta f_{injyx} = 10$ GHz, (d) $\Delta f_x = 0$ GHz, (e) $\Delta f_x = 5$ GHz, (f) $\Delta f_x = 10$ GHz.

for the case of $\Delta f_{injyx} = 5$ GHz are smaller than those for $\Delta f_{injyx} = 0$ GHz, which verifies the results shown in Figure 3.

Additionally, Figure 5 displays the maps of $I_{xm} - I_{ym}$ in the two-dimensional space of k_{injx} and E_{cwx} for six different combinations of Δf_x and Δf_{injyx} . Here, we consider $k_{injx} = k_{injy}$. Obviously, the PS point locates at a lower E_{cws} for a larger k_{injx} . Besides, for a given k_{injx} , a larger Δf_{injyx} leads to a smaller E_{cwx} corresponding to the PS point, while a larger Δf_x leads to a higher E_{cwx} corresponding to the PS point. For instance, for $k_{injx} = 100 \text{ ns}^{-1}$, the PS points are $E_{cwx} = 0.7$, $E_{cwx} = 0.75$, $E_{cwx} = 0.8$ for $\Delta f_x = 0$ GHz, $\Delta f_x = 5$ GHz, and $\Delta f_x = 10$ GHz, respectively.

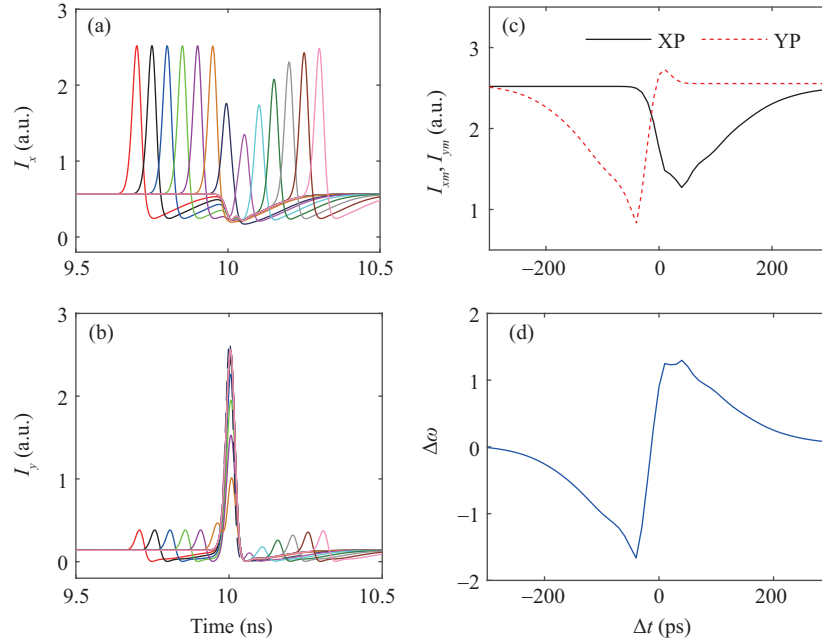


Figure 6 (Color online) (a) I_x , (b) I_y for some representative Δt , (c) I_{xm} and I_{ym} as functions of Δt , (d) the calculated STDP curve, with $E_{cwx} = 0.65$.

3.2 Optical STDP based on a single VCSEL subject to OPCWOI and DPPOI

Subsequently, we set E_{cwx} to be close to the PS point, and consider the two stimuli pulses with different Δt to explore the feasibility of realizing a real-time optical STDP based on the response spiking dynamics in a single VCSEL.

To numerically calculate the optical STDP curve, we fix $t_y = 10$ ns, and vary t_x in the range from 9.2 ns to 10.3 ns [42]. The response spiking dynamics of the VCSEL for different Δt are presented in Figures 6(a) and (b). The values of I_{xm} and I_{ym} as functions of Δt are also presented in Figure 6(c). Obviously, when $\Delta t < 0$, i.e., $t_x < t_y = 10$ ns, the value of I_{xm} keeps around a constant value that is close to the maximum, as this output spike is triggered by the preceding stimulus pulse [42]. While I_{ym} decreases with the increase of Δt , as the carriers consumed by the preceding stimulus pulse are not completely recovered in a short time period. With the further increase of Δt , as can be clearly seen in Figure 6(c), I_{xm} decreases sharply to the minimum, and meanwhile, I_{ym} increases substantially to the maximum when Δt is near to 0. When $\Delta t > 0$, i.e., $t_x > t_y$, I_{ym} is almost constant around the maximum, while I_{xm} increases with the further increase of Δt until it reaches the maximum owing to the carriers recovery.

With the help of the varying spike amplitudes relationship for different Δt as shown in Figures 6(a) and (b), the synaptic weight update can be simply calculated as

$$\Delta\omega(\Delta t) = I_{ym}(\Delta t) - I_{xm}(\Delta t). \quad (5)$$

The values of calculated $\Delta\omega$ are presented in Figure 6(d). Obviously, the STDP curve is obtained. The learning window is about 600 ps, which is determined by the carrier recovery time of the VCSEL. Interestingly, the calculated real-time STDP curve is similar to the measured data in the biological experiments, but the learning speed is much faster [35,36]. Besides, this calculated real-time STDP curve also agrees well with that obtained by the optical STDP implemented with the conventional SOAs [37–41]. Furthermore, as two polarization modes exhibit spiking dynamics, no additional reference signal is required to calculate $\Delta\omega$, the optical STDP is realized in real-time in a single VCSEL.

The STDP curves for different μ and k_{inj} are presented in Figure 7. Here, the value of E_{cwx} is set to the PS point according to the results in Figures 4 and 5. The values of E_{cwx} are 0.6, 0.65, 0.75 for

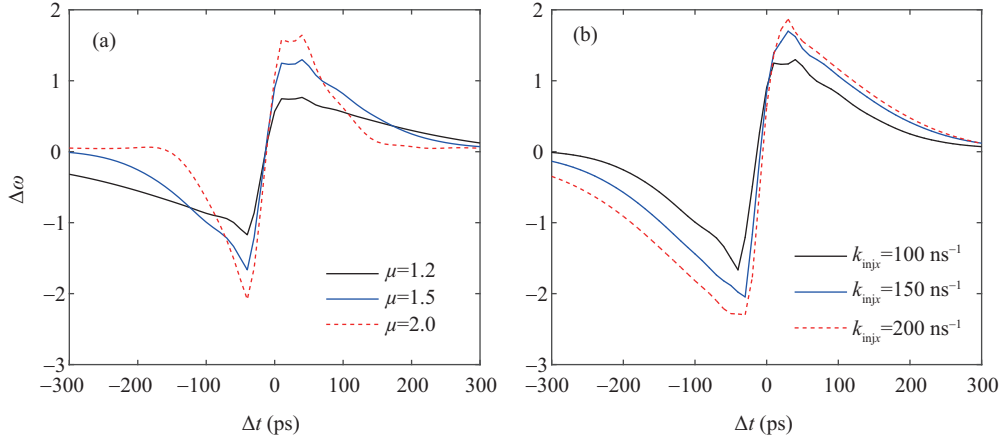


Figure 7 (Color online) The calculated $\Delta\omega$ for (a) different μ with $k_{injx} = k_{in jy} = 100 \text{ ns}^{-1}$, (b) for different k_{injx} with $\mu = 1.5$, with $\Delta f_{injyx} = 0 \text{ GHz}$, $\Delta f_x = -5 \text{ GHz}$.

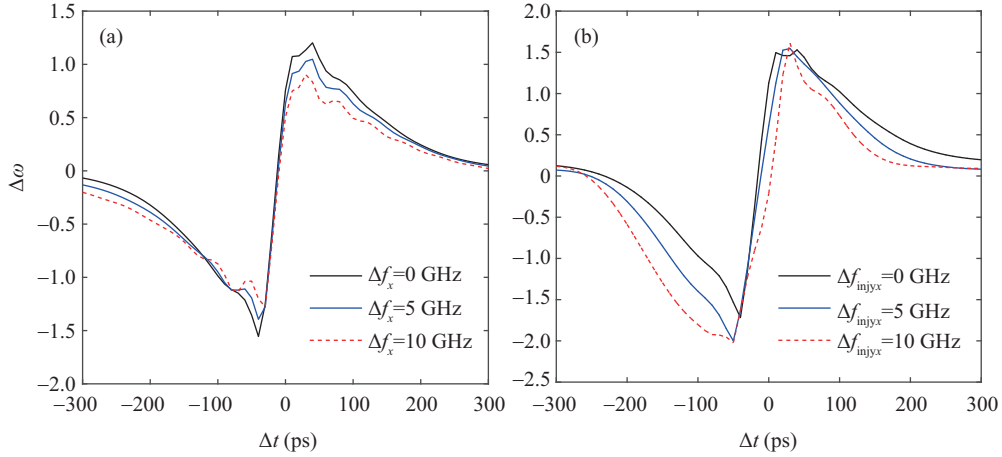


Figure 8 (Color online) The calculated $\Delta\omega$ for (a) different Δf_x with $\Delta f_{injyx} = 0 \text{ GHz}$ and (b) different Δf_{injyx} with $\Delta f_x = -5 \text{ GHz}$.

$\mu = 1.2, 1.5, 2$, and are $0.65, 0.55, 0.5$ for $k_{injx} = 100, 150, 200 \text{ ns}^{-1}$, respectively. It can be observed that, for a larger μ , the height of STDP window is larger whereas the width is smaller, which is similar to the experimental findings based on SOAs [39, 41]. On the other hand, a larger k_{injx} leads to a higher height. But the width of the STDP window is not sensitive to k_{injx} .

Subsequently, the STDP curves for different frequency detuning are depicted in Figure 8. The values of E_{cwx} are set as $0.7, 0.75$ and 0.8 for $\Delta f_x = 0, 5, 10 \text{ GHz}$, respectively, and are set as $0.6, 0.45$ and 0.35 for $\Delta f_{injyx} = 0, 5, 10 \text{ GHz}$, respectively. It can be seen that, the STDP curve can be obtained for all the considered cases of frequency detuning, which is highly desirable for practical application.

At last, we further take into account the VCSEL when it is not operated near the PS point. The parameters are fixed at $\Delta f_{injyx} = 5 \text{ GHz}$, $\Delta f_x = -5 \text{ GHz}$, $k_{injx} = k_{in jy} = 100 \text{ ns}^{-1}$, $\mu = 1.5$. The calculated STDP curves for different E_{cwx} are presented in Figure 9. As can be seen that, when E_{cwx} is set at the PS point, i.e., $E_{cwx} = 0.45$, the potentiation and depression windows are separated by $\Delta\omega = 0$, which is similar to the biological counterpart [35, 36]. For $E_{cwx} = 0.3$, the STDP curve moves to higher values. The potentiation and depression windows are separated by $\Delta\omega = 1$. While for the case of $E_{cwx} = 0.6$, the STDP curve moves to lower values. The potentiation and depression windows are separated by $\Delta\omega = -0.4$. That is to say, the choice of PS point, which leads to similar maximum spike amplitudes in two polarization modes, is critical for achieving the real-time optical STDP.

To explain the STDP properties for different E_{cwx} , the temporal response outputs are further provided in Figure 10. The input stimuli pulses are also displayed in Figure 10(a). For clarity, we consider that

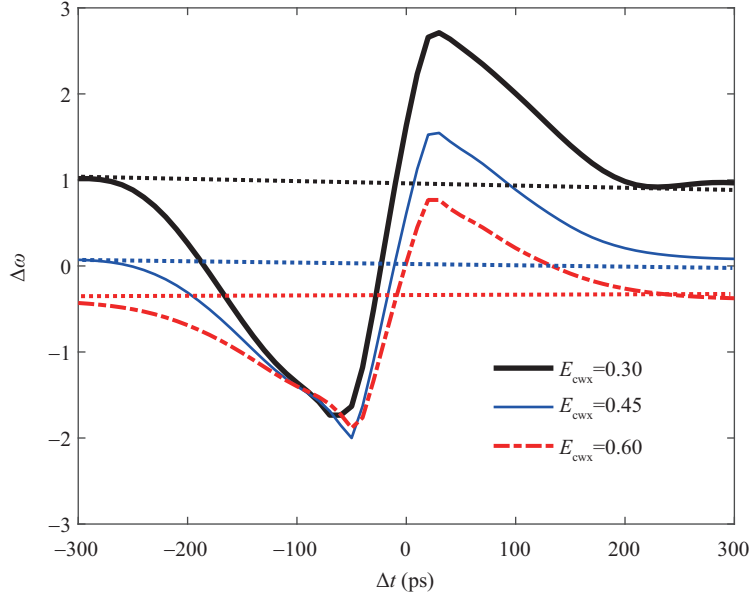


Figure 9 (Color online) The calculated $\Delta\omega$ for different E_{cwx} , with $\Delta f_{injx} = 5$ GHz, $\Delta f_x = -5$ GHz.

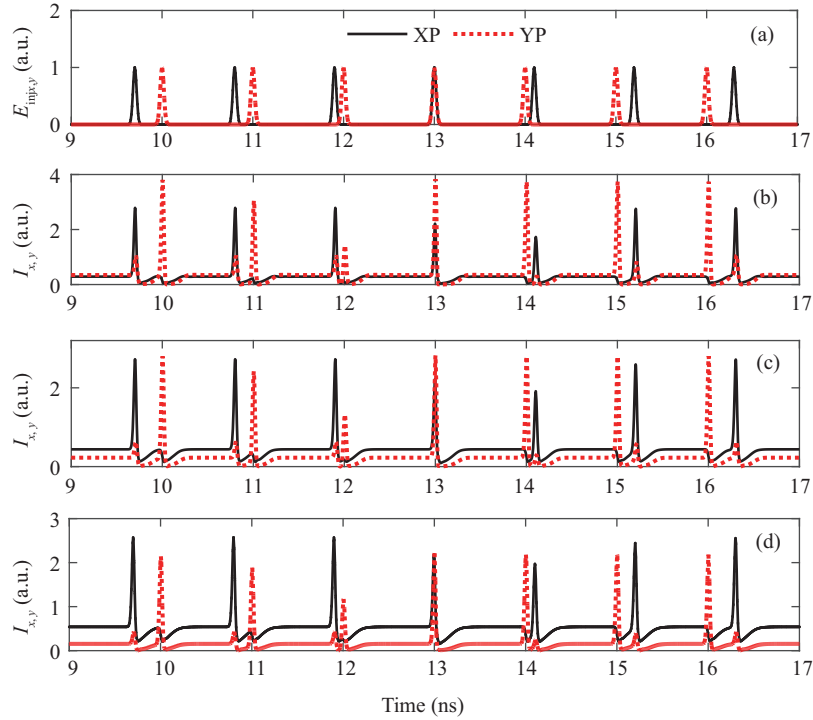


Figure 10 (Color online) (a) Stimuli pulses and responded spikes outputs for (b) $E_{cwx} = 0.3$, (c) $E_{cwx} = 0.45$, and (d) $E_{cwx} = 0.6$, with $\Delta f_{injx} = 5$ GHz, $\Delta f_x = -5$ GHz.

the input stimuli pulses are a train of pre- and post-synaptic spike pairs with seven typical Δt . For $E_{cwx} = 0.3$, we can observe that the maximum of I_{xm} for the seven different Δt is smaller than the maximum of I_{ym} . According to (5), a larger I_{ym} leads to a larger value of $\Delta\omega$. For $E_{cwx} = 0.45$, the maximum of I_{xm} for the seven different Δt is close to the maximum of I_{ym} . For $E_{cwx} = 0.6$, the maximum of I_{xm} is larger than the maximum of I_{ym} , which is responsible for the lower values of STDP curve.

Note that, in a possible experiment, the polarization states of the E_{cwx} , E_{injx} , and $E_{in jy}$ should be carefully controlled to ensure the normal polarization switching and reverse polarization switching, which is critical to the generation of spiking dynamics in two polarization modes. Besides, the precise control

of the strength of E_{cw} is another key factor for the achievement of real-time STDP.

The proposed real-time STDP circuit is a promising candidate for synapse-like element in constructing an all-optical hardware spiking neural network, and has potential applications in ultrafast brain-like computing fields. It exhibits several advantages compared with the preceding photonic STDP circuits. First, it inherits the advantages of low power consumption of VCSEL. Second, the photonic STDP circuit based on VCSEL can be easily integrated with the photonic spiking neurons based on VCSEL, and thus enables constructing a fully-VCSELs-based photonic spiking neural network. Third, it allows calculating photonic STDP curve in real time, which is helpful for designing an on-line learning algorithm.

4 Conclusion

In conclusion, we proposed and numerically demonstrated a real-time optical STDP circuit by using a single VCSEL that is subjected to OPCWOI and DPPOI. Owing to the polarization switching and injection locking effect, the real-time optical STDP can be realized in a single VCSEL by simultaneously using the spiking dynamics in two polarization modes. Besides, the defined PS point, corresponding to the strength of OPCWOI that leads to similar maximum spike amplitudes in two polarization modes, is critical for the real-time optical STDP. Additionally, the optical STDP curve could be slightly controlled by adjusting the bias current, the strength of OPCWOI and DPPOI. The STDP curve can still be achieved even with different frequency detuning, which is important for a practical application. The real-time optical STDP based on a single VCSEL is numerically realized for the first time, which could be easily integrated with the VCSELs-based photonic spiking neurons, and hence can potentially enable energy-efficient implementation of fully VCSELs-based photonic neuromorphic computing system.

Acknowledgements This work was supported in part by National Key Research and Development Program of China (Grant No. 2018YFB2200500) and National Natural Science Foundation of China (Grant Nos. 61974177, 61674119).

References

- 1 Prucnal P R, Shastri B J, de Lima T F, et al. Recent progress in semiconductor excitable lasers for photonic spike processing. *Adv Opt Photon*, 2016, 8: 228–299
- 2 Tait A N, Thomas F D L, Zhou E, et al. Neuromorphic photonic networks using silicon photonic weight banks. *Sci Rep*, 2017, 7: 1–10
- 3 de Lima T F, Peng H T, Tait A N, et al. Machine learning with neuromorphic photonics. *J Lightw Technol*, 2019, 37: 1515–1534
- 4 Feldmann J, Youngblood N, Wright C D, et al. All-optical spiking neurosynaptic networks with self-learning capabilities. *Nature*, 2019, 569: 208–214
- 5 Xu S F, Wang J, Wang R, et al. High-accuracy optical convolution unit architecture for convolutional neural networks by cascaded acousto-optical modulator arrays. *Opt Express*, 2019, 27: 19778
- 6 Roy K, Jaiswal A, Panda P. Towards spike-based machine intelligence with neuromorphic computing. *Nature*, 2019, 575: 607–617
- 7 Xiang S Y, Zhang Y H, Gong J K, et al. STDP-based unsupervised spike pattern learning in a photonic spiking neural network with VCSELs and VCISOAs. *IEEE J Sel Top Quantum Electron*, 2019, 25: 1–9
- 8 Robertson J, Wade E, Kopp Y, et al. Toward neuromorphic photonic networks of ultrafast spiking laser neurons. *IEEE J Sel Top Quantum Electron*, 2020, 26: 1–15
- 9 Peng H T, Angelatos G, de Lima T F, et al. Temporal information processing with an integrated laser neuron. *IEEE J Sel Top Quantum Electron*, 2020, 26: 1–9
- 10 Hurtado A, Henning I D, Adams M J. Optical neuron using polarisation switching in a 1550 nm-VCSEL. *Opt Express*, 2010, 18: 25170
- 11 Coomans W, Gelens L, Beri S, et al. Solitary and coupled semiconductor ring lasers as optical spiking neurons. *Phys Rev E*, 2011, 84: 036209
- 12 Barbay S, Kuszelewicz R, Yacomotti A M. Excitability in a semiconductor laser with saturable absorber. *Opt Lett*, 2011, 36: 4476–4478
- 13 Hurtado A, Schires K, Henning I D, et al. Investigation of vertical cavity surface emitting laser dynamics for neuromorphic photonic systems. *Appl Phys Lett*, 2012, 100: 103703

- 14 Romeira B, Javaloyes J, Ironside C N, et al. Excitability and optical pulse generation in semiconductor lasers driven by resonant tunneling diode photo-detectors. *Opt Express*, 2013, 21: 20931–20940
- 15 Nahmias M A, Shastri B J, Tait A N, et al. A leaky integrate-and-fire laser neuron for ultrafast cognitive computing. *IEEE J Sel Top Quantum Electron*, 2013, 19: 1–12
- 16 Alexander K, van Vaerenbergh T, Fiers M, et al. Excitability in optically injected microdisk lasers with phase controlled excitatory and inhibitory response. *Opt Express*, 2013, 21: 26182–26191
- 17 Selmi F, Braive R, Beaudoin G, et al. Relative refractory period in an excitable semiconductor laser. *Phys Rev Lett*, 2014, 112: 183902
- 18 Hurtado A, Javaloyes J. Controllable spiking patterns in long-wavelength vertical cavity surface emitting lasers for neuromorphic photonics systems. *Appl Phys Lett*, 2015, 107: 241103
- 19 Mesaritakis C, Kapsalis A, Bogris A, et al. Artificial neuron based on integrated semiconductor quantum dot mode-locked lasers. *Sci Rep*, 2016, 6: 39317
- 20 Garbin B, Dolcemascolo A, Prati F, et al. Refractory period of an excitable semiconductor laser with optical injection. *Phys Rev E*, 2017, 95: 012214
- 21 Robertson J, Deng T, Javaloyes J, et al. Controlled inhibition of spiking dynamics in VCSELs for neuromorphic photonics: theory and experiments. *Opt Lett*, 2017, 42: 1560–1563
- 22 Xiang S Y, Zhang H, Guo X X, et al. Cascadable neuron-like spiking dynamics in coupled VCSELs subject to orthogonally polarized optical pulse injection. *IEEE J Sel Top Quantum Electron*, 2017, 23: 1–7
- 23 Deng T, Robertson J, Hurtado A. Controlled propagation of spiking dynamics in vertical-cavity surface-emitting lasers: towards neuromorphic photonic networks. *IEEE J Sel Top Quantum Electron*, 2017, 23: 1–8
- 24 Ma P Y, Shastri B J, de Lima T F, et al. All-optical digital-to-spike conversion using a graphene excitable laser. *Opt Express*, 2017, 25: 33504–33513
- 25 Ma P Y, Shastri B J, de Lima T F, et al. Simultaneous excitatory and inhibitory dynamics in an excitable laser. *Opt Lett*, 2018, 43: 3802–3805
- 26 Robertson J, Ackemann T, Lester L F, et al. Externally-triggered activation and inhibition of optical pulsating regimes in quantum-dot mode-locked lasers. *Sci Rep*, 2018, 8: 12515
- 27 Xiang S Y, Zhang Y H, Guo X X, et al. Photonic generation of neuron-like dynamics using VCSELs subject to double polarized optical injection. *J Lightw Technol*, 2018, 36: 4227–4234
- 28 Zhang Y H, Xiang S Y, Guo X X, et al. Polarization-resolved and polarization- multiplexed spike encoding properties in photonic neuron based on VCSEL-SA. *Sci Rep*, 2018, 8: 16095
- 29 Deng T, Robertson J, Wu Z M, et al. Stable propagation of inhibited spiking dynamics in vertical-cavity surface-emitting lasers for neuromorphic photonic networks. *IEEE Access*, 2018, 6: 67951–67958
- 30 Zhang Y H, Xiang S Y, Guo X X, et al. All-optical inhibitory dynamics in photonic neuron based on polarization mode competition in a VCSEL with an embedded saturable absorber. *Opt Lett*, 2019, 44: 1548–1551
- 31 Tait A N, de Lima T F, Nahmias M A, et al. Silicon photonic modulator neuron. *Phys Rev Appl*, 2019, 11: 064043
- 32 Pammi V A, Alfaro-Bittner K, Clerc M G, et al. Photonic computing with single and coupled spiking micropillar lasers. *IEEE J Sel Top Quantum Electron*, 2020, 26: 1–7
- 33 Iga K. Forty years of vertical-cavity surface-emitting laser: invention and innovation. *Jpn J Appl Phys*, 2018, 57: 08PA01
- 34 Jiang B, Wu Z M, Deng T, et al. Polarization switching characteristics of 1550-nm vertical-cavity surface-emitting lasers subject to double polarization pulsed injection. *IEEE J Quantum Electron*, 2016, 52: 1–7
- 35 Bi G Q, Poo M M. Synaptic modifications in cultured hippocampal neurons: dependence on spike timing, synaptic strength, and postsynaptic cell type. *J Neurosci*, 1998, 18: 10464–10472
- 36 Bi G Q, Poo M M. Synaptic modification by correlated activity: Hebb's postulate revisited. *Annu Rev Neurosci*, 2001, 24: 139–166
- 37 Fok M P, Tian Y, Rosenbluth D, et al. Pulse lead/lag timing detection for adaptive feedback and control based on optical spike-timing-dependent plasticity. *Opt Lett*, 2013, 38: 419–421
- 38 Toole R, Fok M P. Photonic implementation of a neuronal algorithm applicable towards angle of arrival detection and localization. *Opt Express*, 2015, 23: 16133–16141
- 39 Ren Q S, Zhang Y L, Wang R, et al. Optical spike-timing-dependent plasticity with weight-dependent learning window and reward modulation. *Opt Express*, 2015, 23: 25247–25258
- 40 Toole R, Tait A N, de Lima T F, et al. Photonic implementation of spike-timing-dependent plasticity and learning algorithms of biological neural systems. *J Lightw Technol*, 2016, 34: 470–476
- 41 Li Q, Wang Z, Le Y S, et al. Optical implementation of neural learning algorithms based on cross-gain modulation in a semiconductor optical amplifier. In: *Proceedings of SPIE*, 2016. 10019
- 42 Xiang S Y, Gong J K, Zhang Y H, et al. Numerical implementation of wavelength-dependent photonic spike timing

- dependent plasticity based on VCISOA. *IEEE J Quantum Electron*, 2018, 54: 1–7
- 43 Martin-Regalado J, Prati F, Miguel M S, et al. Polarization properties of vertical-cavity surface-emitting lasers. *IEEE J Quantum Electron*, 1997, 33: 765–783
- 44 Perez P, Valle A, Pesquera L, et al. All-optical inverter based on polarization switching in VCSELs subject to single and dual optical injection. *IEEE J Sel Top Quantum Electron*, 2013, 19: 1700408
- 45 Xiang S Y, Pan W, Luo B, et al. Influence of variable-polarization optical feedback on polarization switching properties of mutually coupled VCSELs. *IEEE J Sel Top Quantum Electron*, 2013, 19: 1700108
- 46 Salvide M F, Torre M S, Henning I D, et al. Dynamics of normal and reverse polarization switching in 1550-nm VCSELs under single and double optical injection. *IEEE J Sel Top Quantum Electron*, 2015, 21: 643–651
- 47 Jiang N, Xue C, Liu D, et al. Secure key distribution based on chaos synchronization of VCSELs subject to symmetric random-polarization optical injection. *Opt Lett*, 2017, 42: 1055–1058
- 48 Li N Q, Susanto H, Cemlyn B R, et al. Stability and bifurcation analysis of spin-polarized vertical-cavity surface-emitting lasers. *Phys Rev A*, 2017, 96: 013840
- 49 Jiang N, Wang Y, Zhao A, et al. Simultaneous bandwidth-enhanced and time delay signature-suppressed chaos generation in semiconductor laser subject to feedback from parallel coupling ring resonators. *Opt Express*, 2020, 28: 1999
- 50 Xiang S Y, Ren Z X, Zhang Y H, et al. All-optical neuromorphic XOR operation with inhibitory dynamics of a single photonic spiking neuron based on a VCSEL-SA. *Opt Lett*, 2020, 45: 1104–1107